Vol. 27 • No. 40 • October 26 • 2017

www.afm-journal.de

ADVANCED FUNCTIONAL MATERIALS

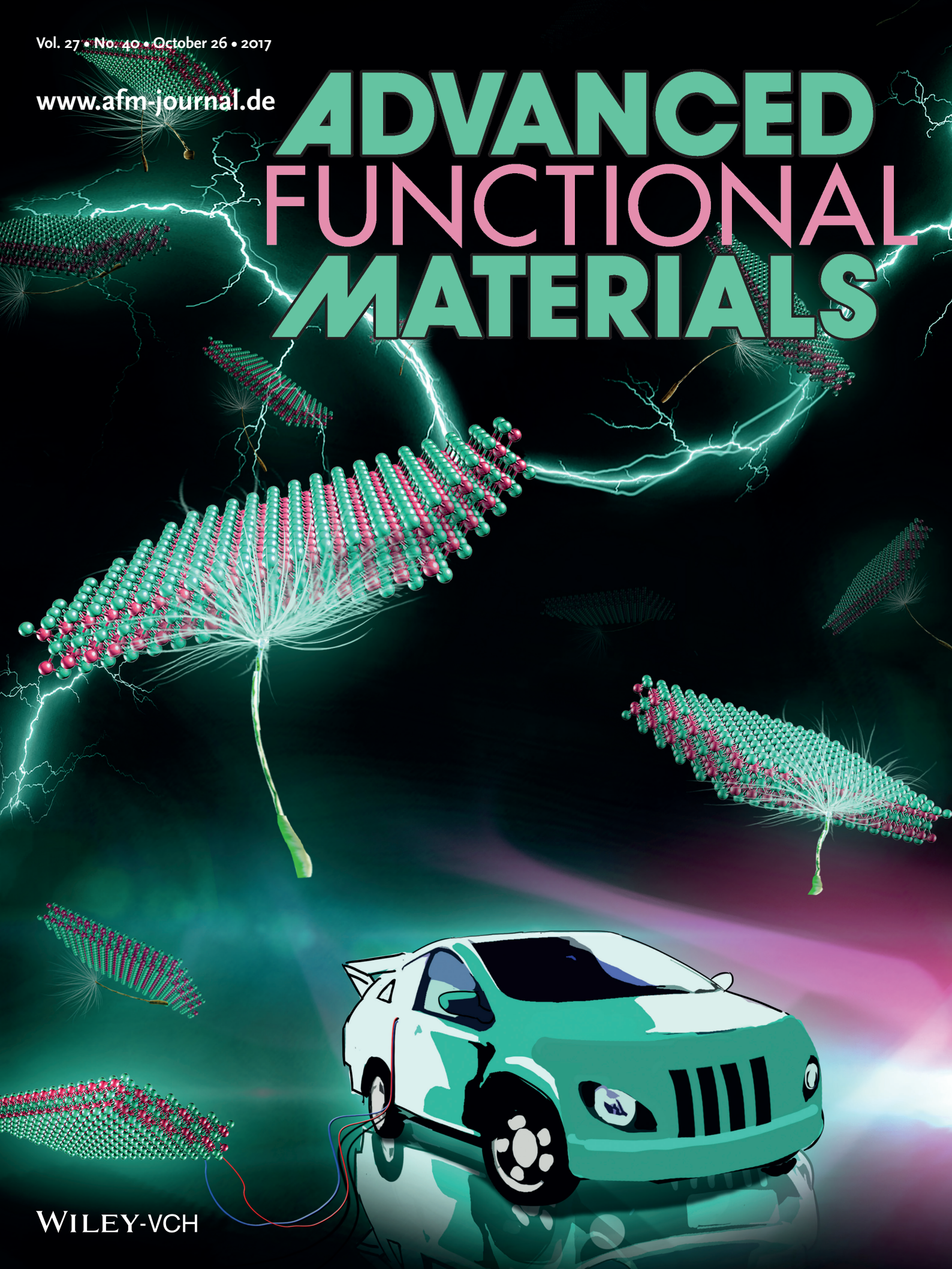

WILEY-VCH

ADVANCED FUNCTIONAL MATERIALS
www.afm-journal.de

Freestanding Metallic 1T MoS_2 with Dual Ion Diffusion Paths as High Rate Anode for Sodium-Ion Batteries

*Xiumei Geng, Yucong Jiao, Yang Han, Alolika Mukhopadhyay, Lei Yang, and Hongli Zhu**

This work studies for the first time the metallic 1T MoS_2 sandwich grown on graphene tube as a freestanding intercalation anode for promising sodium-ion batteries (SIBs). Sodium is earth-abundant and readily accessible. Compared to lithium, the main challenge of sodium-ion batteries is its sluggish ion diffusion kinetic. The freestanding, porous, hollow structure of the electrode allows maximum electrolyte accessibility to benefit the transportation of Na^+ ions. Meanwhile, the metallic MoS_2 provides excellent electron conductivity. The obtained 1T MoS_2 electrode exhibits excellent electrochemical performance: a high reversible capacity of 313 mAh g^{-1} at a current density of 0.05 A g^{-1} after 200 cycles and a high rate capability of 175 mAh g^{-1} at 2 A g^{-1}. The underlying mechanism of high rate performance of 1T MoS_2 for SIBs is the high electrical conductivity and excellent ion accessibility. This study sheds light on using the 1T MoS_2 as a novel anode for SIBs.

1. Introduction

Layered semiconducting trigonal 2H MoS_2 has been investigated as an anode material because of its high theoretical capacity of ≈670 mAh g^{-1} with Na^+ intercalation.[1,2] Despite the high capacity, 2H MoS_2 has poor intrinsic conductivity with a direct band gap of ≈1.9 eV.[3] Furthermore, the 2H MoS_2 electrodes experience structure pulverization and particle aggregation, resulting in poor rate performance and cycling stability.[4–7] Recently, metallic 1T MoS_2 nanosheets have been investigated due to their excellent properties in electrocatalysts,[8,9] photocatalysts,[10] photoelectrochemical cells,[11–13] and supercapacitors.[14,15] Compared to 2H MoS_2, 1T-MoS_2 has two unique structural characteristics that facilitate both electron transport and ion diffusion for electrochemical energy storage technologies: one is the distorted octahedral coordination that makes it an electronic conductor with conductivity ≈10^5 times higher than the 2H phase[16] and the other is high hydrophilicity.[17] High electron conductivity associates the electron transfer, and the hydrophilic property benefits the ion diffusion. These distinct features make 1T MoS_2 an emerging competitive metallic nanosheets for energy storage. However, according to the previous reports, 1T-MoS_2 does not exist in nature but can be prepared with the intercalation of guest ions such as *n*-butyllithium, which easily catches fire on exposure to air. Herein, for the first time, a facile method was developed to in situ synthesize a thin layer of 1T metallic MoS_2 onto both the interior and exterior surfaces of a hollow graphene tube to form 3D MoS_2-graphene sandwich structure. Corresponding electrochemical performance as a freestanding and binder free Na^+-intercalation anode constituent was evaluated.

Sodium-ion batteries (SIBs) are one of the highly promising options for use in next generation large-scale energy storage due to sodium's earth abundance and ready accessibility.[18–21] However, compared to the lithium sodium ion has much slower diffusion kinetics due to the larger size of the Na ion (372% larger in volume than Li ion owing to its higher coordination number of four and the atomic radius of sodium is 99 pm, whereas the atomic radius of lithium is 59 pm).[22] Therefore, there is an urgent need to design a robust and enhanced structure to assist the ion diffusion in SIBs with improved rate performance, capacity, and stability.[18,23–26] To solve the sluggish sodium-ion diffusion kinetics, this work grew the 1T MoS_2 onto the porous 3D hollow graphene foam to increase the ion accessibility. In order to grow a thin layer of 1T MoS_2, onto both the interior and exterior walls of a 3D hollow graphene tube scaffold, ethanol was used as a solvent. Due to the low surface energy of ethanol compared to water, it is more compatible with graphene. The configuration of the two thin layers of 1T MoS_2 sandwiching one inner graphene layer possesses several advantages: (1) provide dual sodium-ion diffusion paths, (2) significantly increase the amount of active material loading per footprint area, and (3) offer mechanical support to the 1T MoS_2 and enable a freestanding electrode without the addition of any binder and conductive additive.

Even though 2H semiconducting MoS_2 has been investigated for Li^+ intercalation, water splitting, and catalysis,[27–30] this is the first application of 1T MoS_2 for Na^+ intercalation. The obtained 1T MoS_2 electrode has a high reversible capacity of 313 mAh g^{-1} at a current density of 0.05 A g^{-1} after 200 cycles and a capability of 175 mAh g^{-1} at a high current density of 2 A g^{-1}. The earth abundance of sodium along with the unique configuration of the MoS_2-graphene electrode

Dr. X. Geng, Dr. Y. Jiao, Y. Han, A. Mukhopadhyay, L. Yang, Prof. H. Zhu
Department of Mechanical Engineering
Northeastern University
Boston, MA 02115, USA
E-mail: h.zhu@neu.edu

DOI: 10.1002/adfm.201702998

presented in this work will shed light on developing metallic MoS_2 for SIBs.

2. Results and Discussion

The fabrication process of the 1T MoS_2 grown on graphene scaffold is illustrated schematically in **Figure 1**. First, graphene was deposited onto nickel foam via chemical vapor deposition (Figure 1a,b). The nickel was etched away with $FeCl_3$ to obtain a transparent, 3D, and hollow graphene microtube scaffold (Figure 1c) with a fraction of surface pores and slits. A solution consisting of MoO_3 and thioacetamide precursors dispersed in ethanol was used to grow the MoS_2. The synthesis procedure was further explained in the Experimental Section. As a result, a thin layer of 1T MoS_2 nucleated on both the interior and exterior surfaces of the graphene tubes and formed a sandwich structure (Figure 1d). This process is the first demonstration of the ability to create a uniform coating of a 1T MoS_2 species onto a 3D graphene surface. The hollow graphene scaffold serves as the backbone for the active 1T MoS_2 layers. Ethanol was chosen as the solvent because the surface energy matches that of graphene allowing the solution to penetrate and wet the entire, especially the interior, wall of graphene scaffold. Also, ethanol is relative environmental friendly organic solvent than *N*,*N*-dimethylformamide, *N*-methyl-2-pyrrolidone, and acetone.[31] The proposed strategy of selecting a solvent, which is compatible with the graphene, is outlined in Figure 1e. The sandwiched graphene layer provides fast electron transport, whereas, the electrolyte that has penetrated into the percolating tube network provides ion diffusion pathways for both 1T MoS_2 layers. The structure of the freestanding MoS_2–graphene–MoS_2 anode supported by a dandelion is graphically illustrated in Figure 1f. It was also evident that the entire structure, as shown in Figure 1f, was very light. It is worth noting that the existence of the multilayers of graphene has no contribution in Na^+ storage due to its limited layer distance, which was further verified in **Figure 2**d.

X-ray photoelectron spectroscopy (XPS), X-ray diffraction (XRD), and Raman spectroscopy were used to analyze the chemical composition of MoS_2 deposited onto the graphene scaffold. The signals observed at 228.8 and 231.9 eV in Mo 3d XPS are corresponding to the $3_{d5/2}$ and $3d_{3/2}$ components of Mo—S bonding in 1T MoS_2 that is ≈1 eV lower with respect to the corresponding 2H MoS_2 peaks.[16] Besides, the Mo—O signal at 235.2 eV is due to tiny amount of unreacted MoO_3. The S 2p XPS signals at 161.5 eV and 162.5 eV, which also confirmed the presence of Mo—S bonding, are associated with S $2P_{3/2}$ and $2P_{1/2}$, respectively. The peaks are also ≈1 eV lower than the peaks in 2H MoS_2 according to the literature.[16] The absence of any S—O bonding in the spectrum indicated that there is no $MoOS_x$ configuration in the material (Figure 2b).[29] Correspondingly, three strong peaks were also observed at 184, 324, and 416 cm^{-1} in Raman spectrum, which is evidently different with the typical Raman shifts at 378 and 404 cm^{-1} of 2H MoS_2. The peak at 184 cm^{-1} is a typical metal–metal Raman stretching mode. According to the previous reports,[16,32–34] the intense peaks at 184 and 324 cm^{-1} are corresponding to

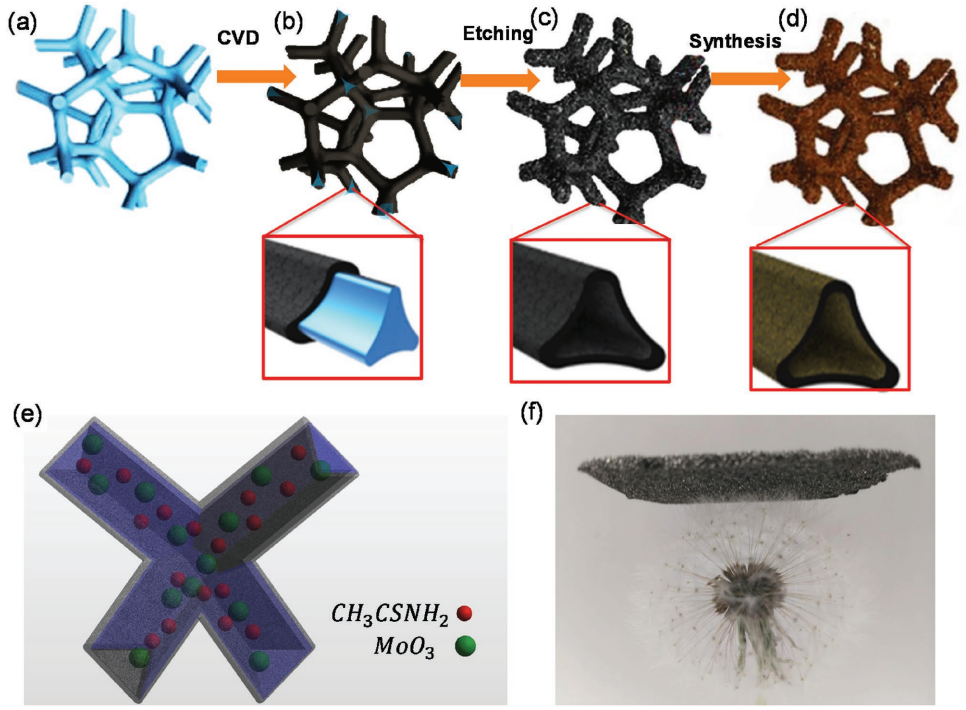

Figure 1. Schematic diagram illustrating the hydrothermal preparation of the 3D MoS_2–graphene–MoS_2 structure. a) A 3D nickel foam. b) Graphene was deposited onto a 3D nickel foam. c) Nickel was etched away to obtain a transparent and hollow graphene foam structure. d) The graphene structure immersed in a precursor solution. 1T MoS_2 grown on the interior and exterior graphene surfaces facilitated by similar surface energies of graphene and ethanol. e) Mechanism of MoS_2 growth on both sides of the 3D graphene. Red dot indicates thioacetamide and green dot indicates MoO_3. f) The lightweight, freestanding MoS_2–graphene foam rested on the top of a dandelion.

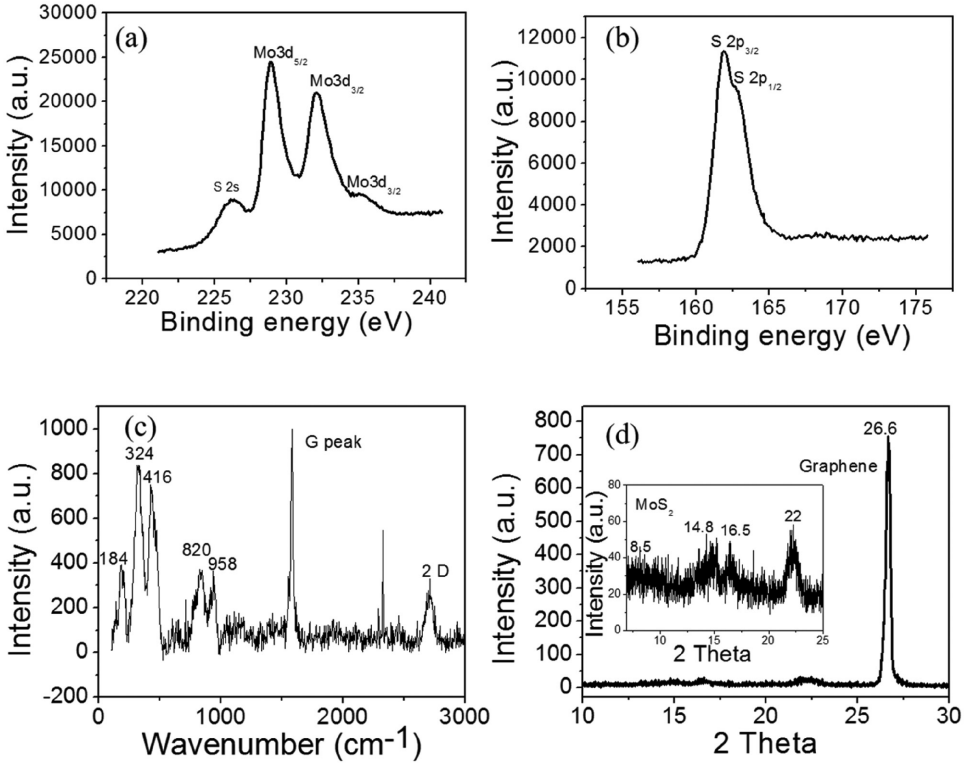

Figure 2. Structural and chemical characterization of the synthesized MoS_2–graphene. XPS spectra of Mo 3d (a) and S 2p (b). c) Raman spectroscopy and d) XRD of MoS_2–graphene.

the typical J1 and J3 peaks of the 1T MoS_2, which indicated that 1T MoS_2 was obtained in this study. Very small amount of MoO_3 in the as-grown MoS_2 layer is also confirmed by their vibration at 820 and 958 cm^{-1} in the Raman spectra (Figure 2c).[35] It is important that the graphene scaffold remains intact during the MoS_2 growth process and preserves the mechanical and electronic integrity of the anode structure. The measured XPS spectrum for carbon has a single peak at 284.5 eV, indicating that the sp^2 carbon in graphene does not react during the hydrothermal growth process (Figure S1, Supporting Information). In Figure 2d, the XRD peak of graphene at 26.6° is attributed to the (002) reflection of graphitic carbon, corresponding to the d-spacing of 0.335 nm, which is too small for Na^+ intercalation.[36] The peaks at around 8.5 and 14.8° in an inset of Figure 2d can be indexed to the (002) and (004) planes of 1T MoS_2, which also indicated the as prepared material is 1T MoS_2.[15,33,37] Furthermore, the weak intensity and broad diffraction peaks demonstrate that MoS_2 has a relatively small size and a relatively low crystallinity, which is in good agreement with the observation of the following high-resolution transmission electronic microscopy (HRTEM) images and selected area electron diffraction (SAED) patterns. The peak at around 16.5° is indexed to the residual Ni in the 3D MoS_2–graphene–MoS_2 sandwich structure,[38,39] and the peak at 22° is corresponding to the (110) plane of the residual MoO_3, agreeing well with the Raman result.[40]

We also measured the electronic conductivity of the as observed material. The resistivity of MoS_2–graphene, measured with a four point probe, was 1.7×10^3 Ω sq^{-1}, which is lower than the pure metallic MoS_2.[16] We believe that the graphene scaffold further improved the conductivity of MoS_2. The morphology of the MoS_2–graphene structure was characterized by both scanning electron microscopy (SEM) and energy dispersive X-ray spectroscopy. **Figure 3**a highlights the continuous network structure of the graphene scaffold, which is necessary for good electron transport within the electrode. A single MoS_2 coated graphene tube is presented in Figure 3b. From this image, it is apparent that both the interior and exterior surface of the tube is covered by a high density of 1T MoS_2. The electrolyte can easily penetrate the graphene scaffold structure and allows for full utilization of the active material on the structure. A high-magnification cross-section image of the graphene tube in Figure 3c reveals the uniform coverage of MoS_2. Growth on both surfaces of the graphene scaffold is a direct consequence of the choice of ethanol as the solvent since the solute precursors can easily access the hydrophobic graphene surface. Planar coverage of MoS_2 on the outer surface of graphene tube is visible in Figure 3d. Elemental mapping of the surface of the MoS_2 layer was performed with energy-dispersive X-ray spectroscopy (EDX) (Figure S2, Supporting Information), and it was found that the Mo and S are evenly distributed throughout the surface region. Furthermore, a uniform coverage of MoS_2 on the inner surface morphology of the graphene tube is indicated in Figure 3e. Sandwich-structured 1T MoS_2–graphene–1T MoS_2 morphology was presented in Figure 3f, in which multilayers of graphene are well defined. The ability of the hydrothermal growth process developed in this work to coat both sides of the graphene substrate is an improvement over previous studies in

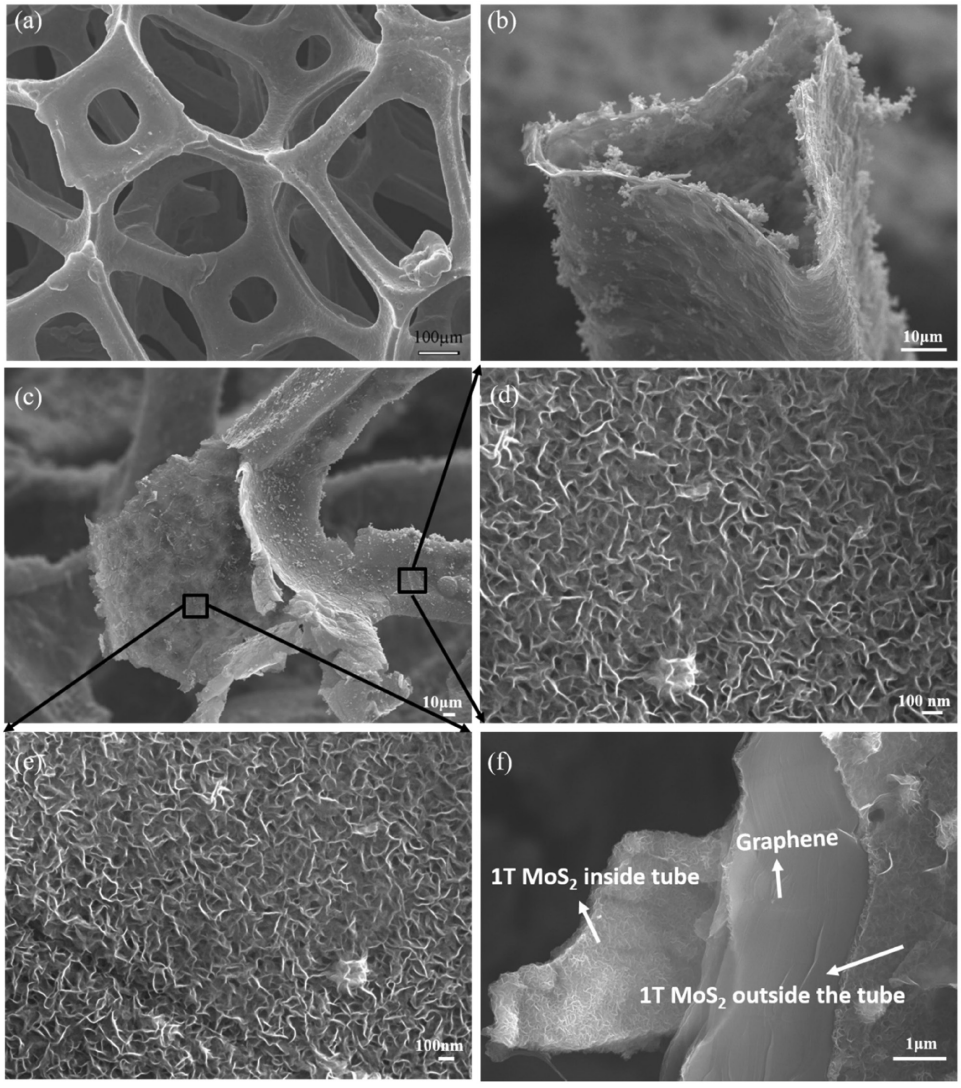

Figure 3. Morphological characterizations of MoS_2 grown on graphene. a) 3D graphene foam structure. b,c) High-magnification image of a double-side-coated graphene tube. d) High-magnification image of 1T MoS_2 on the external surface of the tube. e) High-magnification image of 1T MoS_2 on the internal surface of the tube. f) Cross-section of the edge of a graphene tube.

which active material was only grown on one side of a carbon nanotube,[41] graphene,[1] or nanofiber substrate.[42]

HRTEM observation was prepared by sonicating the MoS_2–graphene material for 10 min. This preparation method highlights the strength of the interaction between the 1T MoS_2 and the graphene substrate as 1T MoS_2 coated graphene was present in HRTEM images (**Figure 4**a,b) and SEM image (Figure S3, Supporting Information). From the uniform intact layer of MoS_2 on graphene after sonication presented in Figure S3 in the Supporting Information, we can see the mechanical bonding between MoS_2 and graphene is robust. The robust mechanical strength attribute to the in situ syntheses procedure in this study. In Figure 4c, we observed the layer distance of the materials on the multilayers graphene at around 0.64–0.65 nm, which is the typical layer distance of few layer MoS_2. Figure 4d shows the SAED pattern of the material on the graphene surface exhibiting hazy and broaden diffraction rings, indicating the material has a low crystalline ratio, which is consistent with the weak and broad peaks of the XRD pattern. The thin, layered structure of the as-prepared MoS_2 is ideal for Na^+ intercalation in an SIBs configuration.

The electrochemical properties of the MoS_2–graphene structure were characterized by galvanostatic cycling and cyclic voltammetry (CV), and the results are presented in **Figure 5**. The galvanostatic charge/discharge curves for 1T MoS_2–graphene electrode cycled between 0.01 and 3.0 V versus Na^+/Na at a current density of 50 mA g^{-1} is plotted in Figure 5a. The initial cycle has a coulombic efficiency of 64%. The voltage plateau at 0.8 V versus Na^+/Na is absent for all the cycles except for the first discharge that can be attributed to the reductive decomposition of electrolyte during the formation of the solid electrolyte interphase (SEI). Voltage plateaus at 1.6 and 1.8 V versus Na^+/Na observed in the subsequent discharge and charge curves, respectively, correspond to the reversible sodium intercalation and deintercalation.

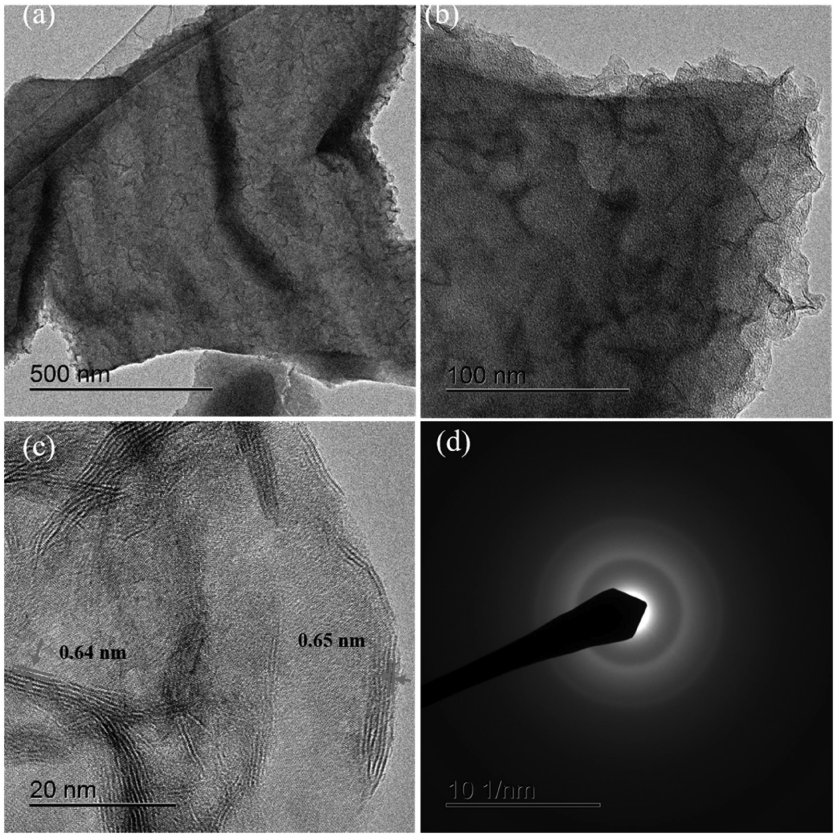

Figure 4. HRTEM characterization. a,b) Low-magnification images, showing a high density of MoS_2 on graphene. c) High-magnification images of MoS_2. d) The selected area electron diffraction (SAED) pattern of MoS_2.

The CV measurements were first performed to determine the reduction and oxidation potentials of the 1T MoS_2–graphene binder-free electrode. The voltammograms of the first five cycles measured between 0.01 and 3.0 V versus Na^+/Na at a scan rate of 0.1 mV s^{-1} are presented in Figure 5b. The strong redox peaks appeared at 1.7 V versus Na^+/Na and weak reduction peak at 0.8 V versus Na^+/Na are also consistent with the voltage plateaus observed during galvanostatic cycling. Clearly, these cathodic and anodic peaks show almost negligible changes in amplitude and voltage positions during the subsequent cycles, indicating an excellent cyclability of the 1T MoS_2–graphene electrode owing to the strong synergistic coupling effects. As can be seen, peaks in the CV curves also prove the as observed material is MoS_2, which proceed in two steps including intercalation and conversion.[2,4,6]

The freestanding electrode architecture provides the 1T MoS_2–graphene–MoS_2 electrode with excellent cycling stability, as seen in the discharge capacity versus cycle number plot in Figure 5c. A high specific capacity of 630 mAh g^{-1} at 50 mA g^{-1} is obtained for the first discharge cycle. After an initial five cycles activation phase, the discharge capacity is around 340 mAh g^{-1} at the 10th cycle and stabilizes at 313 mAh g^{-1} for 200 cycles. The coulombic efficiency of the system with continued cycling is 99%, indicating negligible side reactions during each cycle. For comparison, a separate cell was assembled and cycled using sole graphene foam as the active material. Figure 5c demonstrates that all capacity comes from the 1T MoS_2 since multilayers graphite cannot serve as a sodium anode due to the limited layer distance of 0.34 nm.[36] The high rate capability of the 1T MoS_2–graphene electrode is presented in Figure 5d. The electrode was cycled for ten cycles each at different current densities of 0.5, 0.8, 1.0, 1.5, and 2.0 A g^{-1} and delivered reversible capacities of 241, 222, 208, 190, and 175 mAh g^{-1}, respectively. With an order of magnitude increase in the current density from 0.2 to 2.0 A g^{-1} the capacity decreases to 175 mAh g^{-1}, which is about 62.5% of its original capacity at the low current density (280 mAh g^{-1}). The current density was reduced back to 0.05 A g^{-1} for the final cycle of the rate capability experiment, and the electrode recovers the initial capacity of 313 mAh g^{-1} for five stable cycles. The high rate performance might be due to the combination of the good electronic conductivity of the 1T MoS_2-graphene, the excellent ion diffusion, and electrolyte accessibility of the hollow and porous structure.

The electrochemical impedance spectra (EIS) of the electrodes before and during cycling are compared in Figure 5e. All impedance measurements were made at the fully discharged state. The impedance spectra are combinations of a depressed semicircle in high frequencies and a straight line in low frequencies. In the high-frequency region, the intercepts with real impedance $Z'(\Omega)$ axis being reflected by an ohmic resistance, which includes ionic resistance from the separator paper and electrical resistance from electrodes. It can be seen that the ohmic resistance has a value very near zero, revealing an excellent electrical conductivity of the composite electrode. It is mainly due to the 1T MoS_2 and graphene are both good electronic conductors. The charge transfer resistance of the as assembled cell is quite high; however, after first five cycles, the charge transfer resistance decreases by a factor of five. The charge transfer resistance continues decreasing with cycling and finally stabilizes at the tenth cycle at around 600 Ω. The reduced semicircle indicates a smaller charge transfer resistance, based on which we concluded that the ionic and electronic transfer kinetic is better after the wetting of the electrolyte in the entire graphene foam electrode along with cycling. Furthermore, a stable ion diffusion is evidenced from the similar slope of the Nyquist plot at a lower frequency compared to its initial state. This result is consistent with the cycling performance; the specific discharge capacity stabilized at the tenth cycle and maintained capacity for over 200 cycles. The low impedance of the battery is indicative of the excellent conductivity of the MoS_2–graphene–MoS_2 structure as well as the homogeneous coverage of both surfaces of the graphene tube by 1T MoS_2. Overall, the excellent electrochemical performance of 1T MoS_2–graphene–MoS_2 composite as the Na storage anode can be ascribed to

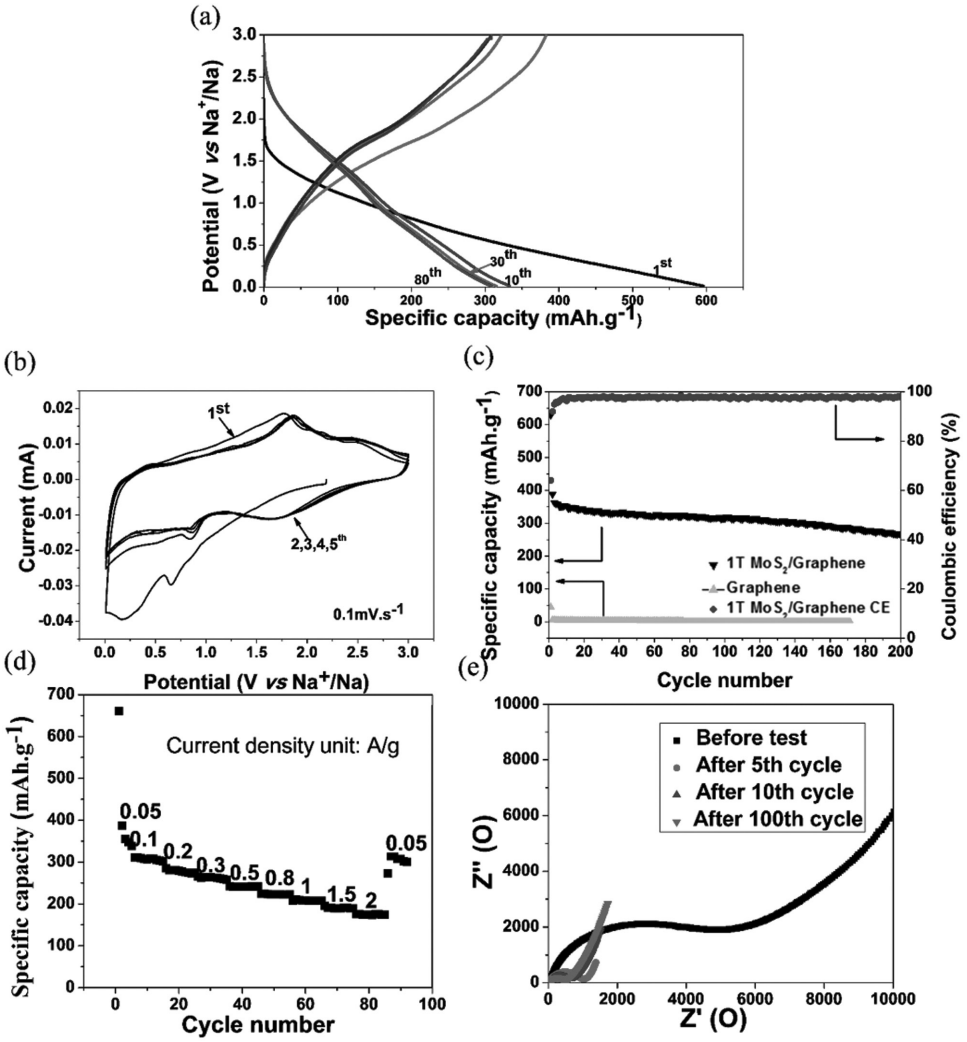

Figure 5. Electrochemical performance. a) Charge/discharge profiles, b) cyclic voltammetry (CV) curves, c) specific capacity and coulombic efficiency versus cycle number at a current density of 50 mA g^{-1}, d) rate performance of the MoS_2-graphene electrode, and e) electrochemical impedance spectra at various cycle numbers.

the synergistic effects of the perfect distribution of highly conductive 1T MoS_2 and graphene foam.

We have also compared the electrochemical performance of 1T MoS_2–graphene with 2H MoS_2–graphene published before.[6] So far the material with the highest capacity was 60-MoS_2–graphene that had an initial capacity of 338 mAh g^{-1} at a current density of 25 mA g^{-1}, and after 20 cycles the capacity became 240 mAh g^{-1}, which is much lower than the 1T MoS_2–graphene material prepared in this research. We speculate that the difference in performance is a result of the high conductivity of 1T MoS_2, which helps the material keep its higher capacity under a high current density. It seems 1T MoS_2–graphene–MoS_2 electrode has a relatively low volumetric energy density because of its porous structure. However, a balance between advantages and disadvantages for the practical application of our prepared nanoactive material in sodium-ion batteries should be carefully considered. The high conductive 1T MoS_2–graphene–MoS_2 electrode with a high rate property and a stable cyclability make it a promising 3D electrode architecture for micro battery applications.

The excellent sodium-ion storage properties of the 1T MoS_2–graphene electrode can be ascribed to their 3D network and high electrical conductivity as well as hollow structure. The 1T MoS_2–graphene functions in the following aspects: (1) the 1T MoS_2 owns high conductivity, which helps the material to keep its high capacity and stability under high current density as a sodium-ion batteries anode; (2) the graphene substrate not only prevents the MoS_2 nanoparticles from aggregating but also provides a conductive matrix to facilitate the electron transportation during the electrode reactions; (3) the 3D hollow nature of MoS_2–graphene enlarges the electrode/electrolyte contact area and further provides an efficient condition for diffusion of electrolyte ion, which improves the rate capability; (4) allows efficient utilization of active material and greatly improves the conductivity and ion diffusion performance without any additional additive. Such long-lasting anode material with high rate capability and stable cyclability can open up a new direction,

which will allow researchers to develop high rate conversion-reaction anodes for high-power sodium-ion batteries for hybrid electric vehicles.

3. Conclusion

For the first time, the metallic 1T MoS_2 was investigated as a high-performance nanostructured anode material for room-temperature sodium-ion batteries. The new material was synthesized on both sides of a freestanding, 3D hollow graphene foam via scalable hydrothermal approach. The unique sandwich structure of the 1T MoS_2–graphene–MoS_2 provides an excellent electrochemical performance, as evidenced by excellent rate capability of 175 mAh g^{-1} at 2 A g^{-1} and a high reversible specific capacity of 313 mAh g^{-1} for 200 cycles. The high conductivity of the 1T MoS_2–graphene–MoS_2 electrode along with the structural configuration of the 3D porous hollow graphene contribute to high rate capability with good electron conductivity and reduced ion diffusion lengths. Meanwhile, the unique configuration prevents the aggregation of MoS_2 nanosheets, whence, possesses excellent cycling stability. This study represents the first application of the metallic 1T MoS_2 for sodium-ion batteries. This general approach for controlling nanostructures can be meaningful in modifying many 2D layered materials to enhance their applications in high-performance energy storage.

4. Experimental Section

Preparation of 3D Graphene Foam: The graphene was synthesized by chemical vapor deposition method with 3D Ni as template and catalyst. First, the 3D Ni foam was heated to 1000 °C in a horizontal tube furnace (MTI corporation) under Ar (500 sccm) and H_2 (200 sccm) atmosphere and annealed for 5 min to eliminate thin surface oxide layer. Then a small amount of CH_4 with the flow rate of 10 sccm was introduced into the reaction tube at ambient pressure. After 5 min of reaction with the gas mixture, the samples were rapidly cooled down to room temperature at a rate of ≈100 °C min^{-1} under Ar (500 sccm) and H_2 (200 sccm) atmosphere. After that, the Ni was etched away with 0.1 M $FeCl_3$ solution till soft and 3D graphene foam suspended in ethanol.

Preparation of 1T MoS_2 Covering 3D Graphene Foam: 12 mg MoO_3 and 24 mg thioacetamide (Fisher Scientific, US) were added into 10 mL ethanol, followed by 1 h magnetic stirring at 500 rpm. Then graphene foam was immersed into the well-distributed solution, transferred to an autoclave and kept in the furnace at 200 °C for 18 h. The autoclave was cooled down to room temperature. The as-prepared MoS_2 on graphene foam was washed with deionized water (DI water) and ethanol individually and dried at 50 °C for 2 h before using it as anode material in sodium-ion battery. The MoS_2–graphene–MoS_2 has an ultra low density of about 0.5 mg cm^{-3}.

Electrochemical Characterization: 2025 coin cells were assembled using 8 × 8 mm^2 1T MoS_2 coated graphene foam as the working electrode. 1 M $NaPF_6$ in (1:1, v/v) ethylene carbonate/dimethyl carbonate with 2% fluoroethylene carbonate (FEC) additive served as the electrolyte. Celgard separator soaked in electrolyte was dropped between the working electrode and sodium metal counter electrode.

All the cycling tests were performed in BT2000 Arbin by sweeping between 3.0 and 0.01 V versus Na/Na^+. Rate performance was tested in the same voltage range with current density increasing consecutively from initial 50 mA g^{-1} to 100, 200, 300, 500, 800, 1000, 1500, and 2000 mA g^{-1} for ten cycles. Finally, the current density was tuned to original 50 mA g^{-1}. Specifically, both Na^+ insertion and extraction were performed under same current density.

Cyclic voltammograms (CVs) were performed using Biologic SP-150 at a scanning rate of 0.1 mV s^{-1}. EIS were tested in the frequency range from 10 mHz to 100 kHz with an amplitude of 5 mV. All the tests were performed at the room temperature.

Physical Characterization: Transmission electron microscopy (TEM) and high-resolution transmission electron microscopy (HRTEM) imaging and electron diffraction were performed on an FEI Tecnai G2 F20 S-Twin microscope operated at an accelerating voltage of up to 200 kV. The TEM samples were prepared by sonication at 500 W for ≈5 min, and 25 µL supernatant was dropped onto holey carbon grids. Morphology and composition of the as-prepared 1T MoS_2 –graphene were characterized by an ultrahigh resolution SEM (Hitachi S4800), which has an optimum resolution of 1.4 nm.

XPS was conducted using an Axis Ultra DLD (Kratos) system. The vacuum of the chamber was 1×10^{-9} Torr. A monochromatic aluminum *K*α source with a source power of 150 W (15 kV × 10 mA) was used. The pass energy was 160 eV for wide scans and 40 eV for narrow scans. Raman spectroscopy was performed using a LabRam HR800 UV NIR and 532 nm laser excitation with working distances on a × 50 lens. The Raman spectra of the 1T MoS_2 –graphene and metallic MoS_2 were recorded by depositing the samples on silicon substrates. The XRD patterns were performed on a Bruker AXS-D8 Advance powder X-ray diffractometer using Cu/Ka radiation (λ = 1.5406 Å) with a step size of 0.02° and a dwell time of 3.0 s.

Supporting Information

Supporting Information is available from the Wiley Online Library or from the author.

Acknowledgements

X.G., Y.J., and Y.H. contributed equally to this work. H.L.Z. acknowledges the financial startup support and Tier 1 support from Northeastern University. The authors acknowledge Dr. K. Xu in Army Research Laboratory, Adelphi, Maryland for providing the electrolyte. The authors thank Dr. Dunwei Wang for sharing his electrochemical test station. The authors also thank the Center for Nanoscale System (CNS) in Harvard University for using their facilities.

Conflict of Interest

The authors declare no conflict of interest.

Keywords

1T MoS_2, anodes, high rate, hollow graphene, sodium-ion batteries

Received: June 3, 2017
Revised: July 16, 2017
Published online: August 25, 2017

[1] X. Cao, Y. Shi, W. Shi, X. Rui, Q. Yan, J. Kong, H. Zhang, *Small* **2013**, *9*, 3433.
[2] J. Wang, C. Luo, T. Gao, A. Langrock, A. C. Mignerey, C. Wang, *Small* **2015**, *11*, 473.

[3] M. Chhowalla, G. A. J. Amaratunga, *Nature* **2000**, *407*, 164.
[4] Y.-X. Wang, K. H. Seng, S.-L. Chou, J.-Z. Wang, Z. Guo, D. Wexler, H.-K. Liu, S.-X. Dou, *Chem. Commun.* **2014**, *50*, 10730.
[5] S. Wei, S. Xu, A. Agrawral, S. Choudhury, Y. Lu, Z. Tu, L. Ma, L. A. Archer, *Nat. Commun.* **2016**, *7*, 11722.
[6] L. David, R. Bhandavat, G. Singh, *ACS Nano* **2014**, *8*, 1759.
[7] F. Zhang, Y. Tang, H. Liu, H. Ji, C. Jiang, J. Zhang, X. Zhang, C. S. Lee, *ACS Appl. Mater. Interfaces* **2016**, *8*, 4691.
[8] Q. Ding, J. Y. Zhai, M. Caban-Acevedo, M. J. Shearer, L. S. Li, H. C. Chang, M. L. Tsai, D. W. Ma, X. W. Zhang, R. J. Hamers, H. He, S. Jin, *Adv. Mater.* **2015**, *27*, 6511.
[9] M. A. Lukowski, A. S. Daniel, F. Meng, A. Forticaux, L. S. Li, S. Jin, *J. Am. Chem. Soc.* **2013**, *135*, 10274.
[10] S. Bai, L. M. Wang, X. Y. Chen, J. T. Du, Y. J. Xiong, *Nano Res.* **2015**, *8*, 175.
[11] E. Aharon, A. Albo, M. Kalina, G. L. Frey, *Adv. Funct. Mater.* **2006**, *16*, 980.
[12] G. Eda, H. Yamaguchi, D. Voiry, T. Fujita, M. W. Chen, M. Chhowalla, *Nano Lett.* **2011**, *11*, 5111.
[13] Q. Ding, F. Meng, C. R. English, M. Caban-Acevedo, M. J. Shearer, D. Liang, A. S. Daniel, R. J. Hamers, S. Jin, *J. Am. Chem. Soc.* **2014**, *136*, 8504.
[14] Y. Yin, P. Miao, Y. M. Zhang, J. C. Han, X. H. Zhang, Y. Gong, L. Gu, C. Y. Xu, T. Yao, P. Xu, Y. Wang, B. Song, S. Jin, *Adv. Funct. Mater.* **2017**, *27*, 1606694.
[15] M. Acerce, D. Voiry, M. Chhowalla, *Nat. Nanotechnol.* **2015**, *10*, 313.
[16] X. Geng, W. Sun, W. Wu, B. Chen, A. Al-Hilo, M. Benamara, H. Zhu, F. Watanabe, J. Cui, T. P. Chen, *Nat. Commun.* **2016**, *7*, 10672.
[17] X. M. Geng, Y. L. Zhang, Y. Han, J. X. Li, L. Yang, M. Benamara, L. Chen, H. L. Zhu, *Nano Lett.* **2017**, *17*, 1825.
[18] S. Y. Hong, Y. Kim, Y. Park, A. Choi, N.-S. Choi, K. T. Lee, *Energy Environ. Sci.* **2013**, *6*, 2067.
[19] W. Luo, F. Shen, C. Bommier, H. Zhu, X. Ji, L. Hu, *Acc. Chem. Res.* **2016**, *49*, 231.
[20] M. Sawicki, L. L. Shaw, *RSC Adv.* **2015**, *5*, 53129.
[21] J. Tang, A. D. Dysart, V. G. Pol, *Curr. Opin. Chem. Eng.* **2015**, *9*, 34.
[22] H. Zhu, Z. Jia, Y. Chen, N. Weadock, J. Wan, O. Vaaland, X. Han, T. Li, L. Hu, *Nano Lett.* **2013**, *13*, 3093.
[23] C. Bommier, T. W. Surta, M. Dolgos, X. Ji, *Nano Lett.* **2015**, *15*, 5888.
[24] H. Kang, Y. Liu, K. Cao, Y. Zhao, L. Jiao, Y. Wang, H. Yuan, *J. Mater. Chem.* **2015**, *3*, 17899.
[25] W. Luo, M. Allen, V. Raju, X. Ji, *Adv. Energy Mater.* **2014**, *4*, 1400554.
[26] C.-Y. Yu, J.-S. Park, H.-G. Jung, K.-Y. Chung, D. Aurbach, Y.-K. Sun, S.-T. Myung, *Energy Environ. Sci.* **2015**, *8*, 2019.
[27] K. Abraham, D. Pasquariello, *Chem. Mater.* **1993**, *5*, 1233.
[28] X.-Q. Bao, D. Y. Petrovykh, P. Alpuim, D. G. Stroppa, N. Guldris, H. Fonseca, M. Costa, J. Gaspar, C. Jin, L. Liu, *Nano Energy* **2015**, *16*, 130.
[29] L. Benoist, D. Gonbeau, G. Pfister-Guillouzo, E. Schmidt, G. Meunier, A. Levasseur, *Solid State Ionics* **1995**, *76*, 81.
[30] D. Genuit, I. Bezverkhyy, P. Afanasiev, *J. Solid State Electrochem.* **2005**, *178*, 2759.
[31] D. W. Johnson, B. P. Dobson, K. S. Coleman, *Curr. Opin. Colloid Interface Sci.* **2015**, *20*, 367.
[32] Q. Liu, X. L. Li, Q. He, A. Khalil, D. B. Liu, T. Xiang, X. J. Wu, L. Song, *Small* **2015**, *11*, 5556.
[33] A. A. Jeffery, S. R. Rao, M. Rajamathi, *Carbon* **2017**, *112*, 8.
[34] J. J. Wu, M. J. Liu, K. Chatterjee, K. P. Hackenberg, J. F. Shen, X. L. Zou, Y. Yan, J. Gu, Y. C. Yang, J. Lou, P. M. Ajayan, *Adv. Mater. Interfaces* **2016**, *3*, 1500669.
[35] D. B. Xiao, J. Y. Zhang, X. Li, D. Zhao, H. Y. Huang, J. L. Huang, D. X. Cao, Z. H. Li, C. M. Niu, *ACS Nano* **2016**, *10*, 9509.
[36] Y. Wen, K. He, Y. J. Zhu, F. D. Han, Y. H. Xu, I. Matsuda, Y. Ishii, J. Cumings, C. S. Wang, *Nat. Commun.* **2014**, *5*, 5033.
[37] K. Chang, W. Chen, *ACS Nano* **2011**, *5*, 4720.
[38] Y. G. Liu, X. H. Wang, H. Z. Liu, Z. H. Dong, S. Q. Li, H. W. Ge, M. Yan, *Energy* **2015**, *84*, 714.
[39] Z. R. Hu, G. Q. Tong, D. Lin, Q. Nian, J. Y. Shao, Y. W. Hu, M. Saei, S. Y. Jin, G. J. Cheng, *J. Mater. Process. Technol.* **2016**, *231*, 143.
[40] N. Illyaskutty, S. Sreedhar, G. S. Kumar, H. Kohler, M. Schwotzer, C. Natzeck, V. P. M. Pillai, *Nanoscale* **2014**, *6*, 13882.
[41] X. Q. Zhang, X. N. Li, J. W. Liang, Y. C. Zhu, Y. T. Qian, *Small* **2016**, *12*, 2484.
[42] X. Xiong, W. Luo, X. Hu, C. Chen, L. Qie, D. Hou, Y. Huang, *Sci. Rep.* **2015**, *5*, 9254.